

REVIEW ARTICLE

Open Access



# Simulating Gaussian boson sampling quantum computers

Alexander S. Dellios<sup>1</sup>, Margaret D. Reid<sup>1</sup> and Peter D. Drummond<sup>1\*</sup> 

## Abstract

A growing cohort of experimental linear photonic networks implementing Gaussian boson sampling (GBS) have now claimed quantum advantage. However, many open questions remain on how to effectively verify these experimental results, as scalable methods are needed that fully capture the rich array of quantum correlations generated by these photonic quantum computers. In this paper, we briefly review recent theoretical methods to simulate experimental GBS networks. We focus mostly on methods that use phase-space representations of quantum mechanics, as these methods are highly scalable and can be used to validate experimental outputs and claims of quantum advantage for a variety of input states, ranging from the ideal pure squeezed vacuum state to more realistic thermalized squeezed states. A brief overview of the theory of GBS, recent experiments, and other types of methods are also presented. Although this is not an exhaustive review, we aim to provide a brief introduction to phase-space methods applied to linear photonic networks to encourage further theoretical investigations.

## 1 Introduction

Since Feynman's original proposal in the early 1980s [1], a growing amount of research has been conducted to develop large-scale, programmable quantum computers that promise to solve classically intractable problems. Although a variety of systems have been proposed to achieve this [2–5], practical issues such as noise and losses introduce errors that scale with system size, hampering physical implementations. Therefore, one approach of current experimental efforts has been the development of specialized devices aiming to unequivocally demonstrate quantum advantage, even when experimental imperfections are present.

To this end, recent developments use photonic networks implementing different computationally hard tasks [6–9]. Such devices are made entirely from linear optics such as polarizing beamsplitters, mirrors, and

phase-shifters [4, 10], with optical parametric oscillators as the quantum source [11, 12]. Unlike cryogenic devices based on superconducting quantum logic gates [13, 14], these networks are operated at room temperature. Large size networks now claim quantum advantage [15–18], especially for a type of quantum computer called a Gaussian boson sampler that generates random bit outputs with a distribution that is exponentially hard to replicate at large network sizes.

This begs the question: how can one verify that large-scale experimental outputs are correct, when the device is designed to solve problems that no classical computer can solve in less than exponential time?

In this paper, we review theoretical methods that answer this for photonic network-based quantum computers. We especially focus on positive-P phase-space representations that can simulate non-classical states [19]. Here, we mean simulate in the sense of a classical sampling algorithm that replicates probabilities and moments to an accuracy better than experimental sampling errors, for the same number of samples. Such methods account for loss and decoherence. They are classical algorithms for standard digital computers. In addition,

\*Correspondence:

Peter D. Drummond  
peterddrummond@protonmail.com

<sup>1</sup> Centre for Quantum Science and Technology Theory, Swinburne University of Technology, Melbourne 3122, Australia

they are highly scalable, with polynomial run-time for large networks.

Other types of simulation exist, where the classical algorithm replicates the detection events of the experiment [20–22]. These become intractably slow for larger networks. The use of methods like this is to offer a way to define quantum advantage, meaning a quantum device performing tasks that are classically infeasible. Hence, we review the definitions of simulation in the literature including other approaches as well. There are also methods that simulate events quickly but approximately, up to a systematic error caused by the fact that the approximate method has a different probability distribution [23–25]. A comparison is made of different approaches that are proposed or used for these problems, including classical “faking” methods that replicate stochastic detection events with some degree of inaccuracy.

Positive-P methods are exactly equivalent to quantum moments in the large sample limit and are applicable to a variety of experimental networks. One example is the coherent Ising machine (CIM) [26, 27], which is used to solve  $NP$ -hard optimization problems by simulating an Ising model with a series of light pulses [9, 28, 29]. The largest experimental implementation of the CIM to date contains 100,000 modes [12]. This gives approximate solutions to hard max-cut problems three orders of magnitude faster than a digital computer. For such problems, typically no exact results are known. Therefore, these solutions can be hard to validate as well.

Gaussian boson sampling [30–32] experiments have seen impressive advancements in recent years. These specialized linear network quantum computers are used as random number generators, where the detected output photon counts correspond to sampling from the  $\#P$ -hard Hafnian or Torontonian distributions [7, 8, 33], which are either directly or indirectly related to the matrix permanent. While more specialized than quantum circuit devices, they are also somewhat more straightforward to implement and analyze theoretically.

Only a few years after the original theoretical proposals [7, 8, 33], multiple large-scale experiments have implemented GBS, with each claiming quantum advantage [15–18]. This rapid increase in network size has far outpaced direct verification methods [20–22], whilst other approximate methods [23, 24] typically cannot reproduce the higher-order correlations generated in linear photonic networks of this type.

In summary, we review progress on simulating binned correlations or moments of experimental GBS networks using the positive-P phase-space representation [30–32], as well as comparing this with other methods. We find that current experimental results disagree with the ideal, pure squeezed state model. However, agreement

is greatly improved with the inclusion of decoherence in the inputs. When this decoherence is large enough, classical simulation is feasible [34, 35], and quantum advantage is lost. Despite this, recent experimental results demonstrate potential for quantum advantage in some of the reported datasets [32].

In order to present a complete picture, we also review the background theory of GBS, recent large scale experiments [15–18] and other proposed verification algorithms [20–25].

## 2 Gaussian boson sampling: a brief overview

The original boson sampler introduced by Aaronson and Arkhipov [6] proposed a quantum computer that generates photon count patterns by randomly sampling an output state whose distribution corresponds to the matrix permanent. The computational complexity arises from sampling the permanent, which is a  $\#P$ -hard computational problem [36, 37].

However, practical applications of the original proposal have seen limited experimental implementations, since they require one to generate large numbers of indistinguishable single photon Fock states. Although small scale networks have been implemented [38–40], to reach a computationally interesting regime requires the detection of at least 50 photons [41, 42]. This is challenging to implement experimentally.

To solve this scalability issue, Hamilton et al. [7] proposed replacing the Fock states with Gaussian states, which can be more readily generated at large sizes. These types of quantum computing networks are called Gaussian boson samplers. They still use a non-classical input state, but one that is far easier to generate experimentally than the original proposal of number states.

### 2.1 Squeezed states

In standard GBS,  $N$  single-mode squeezed vacuum states are sent into an  $M$ -mode linear photonic network. If  $N \neq M$ , the remaining  $N - M$  ports are vacuum states. If each input mode is independent, the entire input state is defined via the density matrix

$$\hat{\rho}^{(\text{in})} = \prod_j^M |r_j\rangle\langle r_j|. \quad (1)$$

Here,  $|r_j\rangle = \hat{S}(r_j)|0\rangle$  is the squeezed vacuum state and  $\hat{S}(r_j) = \exp\left(r_j\left(\hat{a}_j^{(\text{in})}\right)^2/2 - r_j\left(\hat{a}_j^{(\text{in})}\right)^2/2\right)$  is the squeezing operator [43–45]. We assume the squeezing phase is zero and  $\hat{a}_j^{(\text{in})}$  ( $\hat{a}_j^{(\text{in})}$ ) is the input creation (annihilation) operator for the  $j$ th mode. The vacuum state  $|0\rangle$  corresponds to setting  $r_j = 0$  in the squeezing operator.

The ideal GBS assumes that inputs are pure squeezed states [46]. These non-classical states are characterized by their quadrature variance and are defined as [47, 48]

$$\begin{aligned} \Delta_{x_j}^2 &= 2(n_j + m_j) + 1 = e^{2r_j} \\ \Delta_{y_j}^2 &= 2(n_j - m_j) + 1 = e^{-2r_j}. \end{aligned} \tag{2}$$

Here,  $\Delta_{x_j}^2 = \langle (\Delta \hat{x}_j)^2 \rangle = \langle \hat{x}_j^2 \rangle - \langle \hat{x}_j \rangle^2$  is the simplified variance notation for the input quadrature operators  $\hat{x}_j = \hat{a}_j^{(in)} + \hat{a}_j^{\dagger(in)}$  and  $\hat{y}_j = -i(\hat{a}_j^{(in)} - \hat{a}_j^{\dagger(in)})$ , which obey the commutation relation  $[\hat{x}_j, \hat{y}_k] = 2i\delta_{jk}$ .

Squeezed states, while still satisfying the Heisenberg uncertainty principle  $\Delta_{x_j}^2 \Delta_{y_j}^2 = 1$ , have altered variances such that one quadrature has variance below the vacuum noise level,  $\Delta_{x_j}^2 < 1$ . By the Heisenberg uncertainty principle, this causes the variance in the corresponding quadrature to become amplified well above the vacuum limit,  $\Delta_{y_j}^2 > 1$  [43, 49, 50]. Other squeezing orientations are available and remain non-classical so long as one variance is below the vacuum limit.

For pure squeezed states, the number of photons in each mode is  $n_j = \langle \hat{a}_j^{\dagger(in)} \hat{a}_j^{(in)} \rangle = \sinh^2(r_j)$ , whilst the coherence per mode is  $m_j = \langle (\hat{a}_j^{(in)})^2 \rangle = \cosh(r_j) \sinh(r_j) = \sqrt{n_j(n_j + 1)}$ .

### 2.2 Input-output theory

Linear photonic networks made from a series of polarizing beamsplitters, phase shifters and mirrors act as large scale interferometers, and crucially conserve the Gaussian nature of the input state.

In the ideal lossless case, as seen in Fig. 1, photonic networks are defined by an  $M \times M$  Haar random unitary matrix  $\mathbf{U}$ . The term Haar corresponds to the Haar measure, which in general is a uniform probability measure on the elements of a unitary matrix [51].

For lossless networks, input modes are converted to outputs following

$$\hat{a}_k^{(out)} = \sum_{j=1}^M U_{kj} \hat{a}_j^{(in)}, \tag{3}$$

where  $\hat{a}_k^{(out)}$  is the output annihilation operator for the  $k$ th mode. Therefore, each output mode is a linear combination of all input modes.

Practical applications will always include some form of losses in the network, for example, photon absorption. This causes the matrix to become non-unitary, in which case it is denoted by the transmission matrix  $\mathbf{T}$ , and the input-to-output mode conversion now contains additional loss terms [52, 53]:

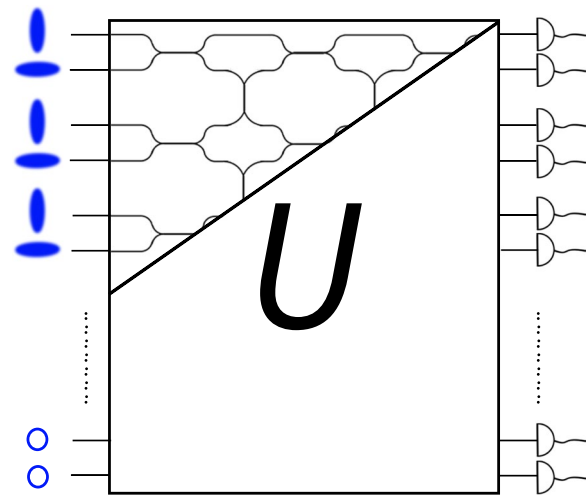


**Fig. 1** Gaussian boson sampling schematic where  $N \subset M$  single-mode squeezed states of different polarizations (blue ellipses) are sent into a lossless linear photonic network where the remaining  $N - M$  inputs are vacuum states (blue outlined circles). The linear network is created from a series of phase-shifters and beamsplitters, represented here in a circuit diagram format. This generates an exponential number of interference pathways. Mathematically, the network is defined by an  $N \times M$  Haar random unitary  $\mathbf{U}$ . Output photon patterns are then obtained using either PNR or click detectors

$$\hat{a}_k^{(out)} = \sum_{j=1}^N T_{kj} \hat{a}_j^{(in)} + \sum_{j=1}^M B_{kj} \hat{b}_j^{(in)}. \tag{4}$$

Here,  $\hat{b}_j^{(in)}$  is the annihilation operator for the  $j$ th loss mode whilst  $\mathbf{B}$  is a random noise matrix. The loss matrix conserves the total unitarity of the system as  $\mathbf{T}\mathbf{T}^\dagger + \mathbf{B}\mathbf{B}^\dagger = \mathbf{I}$ , where  $\mathbf{I}$  is the identity matrix.

Although linear networks are conceptually simple systems, they introduce computational complexity from the exponential number of possible interference pathways photons can take in the network. These are generated from the beamsplitters. As an example, the input ports of a 50/50 beamsplitter are defined as superpositions of the output modes:

$$\begin{aligned} \hat{a}_1^{\dagger(in)} &= \frac{1}{\sqrt{2}} (\hat{a}_3^{\dagger(out)} + \hat{a}_4^{\dagger(out)}) \\ \hat{a}_2^{\dagger(in)} &= \frac{1}{\sqrt{2}} (\hat{a}_3^{\dagger(out)} - \hat{a}_4^{\dagger(out)}). \end{aligned} \tag{5}$$

Classical states such as coherent and thermal states input into large-scale linear networks are readily simulated on a classical computer [34]. This leads to the question, why are non-classical states such as Fock and squeezed states computationally hard to simulate on large-scale photonic networks?

In short, non-classical states input into a linear network generate large amounts of quantum correlations, which are non-trivial to simulate classically if combined with photo-detection. Continuing with the beamsplitter example above, if input ports 1 and 2 now contain indistinguishable Fock states, as is the case with standard boson sampling, the input state can be written as

$$|1, 1\rangle_{1,2} = \frac{1}{\sqrt{2}}(|2, 0\rangle_{3,4} - |0, 2\rangle_{3,4}). \quad (6)$$

The absence of a  $|1, 1\rangle_{3,4} = \hat{a}_3^{\dagger(\text{out})}\hat{a}_4^{\dagger(\text{out})}|0, 0\rangle_{3,4}$  term means the output photons are bunched, that is, they are entangled and always arrive in pairs [54]. This phenomena is known as the Hong-Ou-Mandel (HOM) interference effect and is named after the authors who first observed this phenomena [55].

If input ports 1 and 2 have input-squeezed vacuum states, one generates two-mode Einstein-Podolsky-Rosen (EPR) entanglement in the quadrature-phase amplitudes [56, 57]. More details, including a summary of the derivation, can be found in [31, 58].

### 2.3 Photon counting

In GBS experiments, photon count patterns, denoted by the vector  $\mathbf{c}$ , are generated by measuring the output state  $\hat{\rho}^{(\text{out})}$ . The corresponding distribution changes depending on the type of detector used.

The original proposal for GBS [7] involved normally ordered photon-number-resolving (PNR) detectors that can distinguish between oncoming photons and implement the projection operator [54, 59]

$$\hat{p}_j(\mathbf{c}_j) = \frac{1}{c_j!} : (\hat{n}'_j)^{c_j} e^{-\hat{n}'_j} :. \quad (7)$$

Here,  $: \dots :$  denotes normal ordering,  $c_j = 0, 1, 2, \dots$  is the number of counts in the  $j$ th detector and  $\hat{n}'_j = \hat{a}_j^{\dagger(\text{out})}\hat{a}_j^{(\text{out})}$  is the output photon number. Practically, a PNR detector typically saturates for a maximum number of counts  $c_{\text{max}}$ , the value of which varies depending on the type of PNR detector implemented.

When the mean number of output photons per mode satisfies  $\langle \hat{n}'_j \rangle \ll 1$ , PNR detectors are equivalent to threshold, or click, detectors which saturate for more than one photon at a detector. Click detectors are described by the projection operator [59]

$$\hat{\pi}_j(\mathbf{c}_j) =: e^{-\hat{n}'_j} (e^{\hat{n}'_j} - 1)^{c_j} :, \quad (8)$$

where  $c_j = 0, 1$  regardless of the actual number of photons arriving at the detector.

In situations where  $\langle \hat{n}'_j \rangle \gg 1$ , click detectors cannot accurately discriminate between the different numbers of oncoming photons. However, by sending photons through a demultiplexer (demux) before arriving at the detector, the output pulses of light become "diluted" such that the photon number is small enough to be accurately counted using click detectors [60, 61]. In this approach, the demux acts as a type of secondary optical network of size  $1 \times M_S$ , where  $M_S$  is the number of secondary modes. For output photons to become sufficiently dilute, one must satisfy  $M_S \gg \langle \hat{n}'_j \rangle$  [60–62]. When this is the case, the detectors can be thought of pseudo-PNR (PPNR), because the click detectors are accurately measuring photon counts, thus becoming equivalent to PNR detectors [62].

The computational complexity of GBS arises in the probabilities of count patterns  $\mathbf{c}$ . These probabilities are determined using a straightforward extension of the projection operators for both PNR and click detectors. In the case of PNR detectors, the operator for a specific photon count pattern is

$$\hat{P}(\mathbf{c}) = \bigotimes_{j=1}^M \hat{p}_j(c_j), \quad (9)$$

the expectation value of which corresponds to the  $\#P$ -hard matrix Hafnian [7, 33]

$$\langle \hat{P}(\mathbf{c}) \rangle \approx |\text{Haf}(\mathbf{D}_S)|^2. \quad (10)$$

Here,  $\mathbf{D}_S$  is the sub-matrix of  $\mathbf{D} = \mathbf{T} \left( \bigoplus_{j=1}^M \tanh(r_j) \right) \mathbf{T}^T$ , corresponding to the channels with detected photons, where the superscript  $T$  denotes the transpose of the lossy transmission matrix.

The Hafnian is a more general function than the matrix permanent, although both are related following [7, 33]

$$\text{perm}(\mathbf{D}) = \text{Haf} \begin{pmatrix} 0 & \mathbf{D} \\ \mathbf{D}^T & 0 \end{pmatrix}. \quad (11)$$

Therefore, one of the advantages of GBS with PNR detectors is that one can compute the permanent of large matrices from the Hafnian instead of performing Fock state boson sampling.

For click detectors, the operator for a specific binary count pattern  $\mathbf{c}$  is

$$\hat{\Pi}(\mathbf{c}) = \bigotimes_{j=1}^M \hat{\pi}_j(c_j), \quad (12)$$

whose expectation value corresponds to the Torontonian [8]

$$\langle \hat{\Pi}(c) \rangle = \text{Tor}(\mathbf{O}_S), \quad (13)$$

where  $\mathbf{O}_S$  is a matrix constructed from the covariance matrix of the output state. The Torontonian has also been shown to be  $\#P$ -hard to compute, and is related to the Hafnian [8].

#### 2.4 Experimental progress

Only a few short years after the original proposal of GBS with click detectors [8], the first large-scale experimental network, called Jiuzhang 1.0, was implemented by Zhong et al. [15]. In this experiment, 25 two-mode squeezed states, corresponding to  $N = 50$  single-mode squeezed states, were created by driving nonlinear crystals with transform-limited laser pulses, which is the standard process of parametric down-conversion. The polarization of each input squeezed state alternates from horizontal to vertical for each spatial mode as illustrated in Fig. 1.

Once generated, the squeezed states were sent into a lossy  $M = 100$  mode linear network made from over 300 beamsplitters and phase-shifters. The network is separated into two stages: The first consists of three-dimensional five-layer triangular and rectangular interferometers [63], similar to the network implemented in the Fock state boson sampling experiment of Wang et al. [64]. The squeezed photons propagate through the triangular layers, allowing photons of the same polarization within the same layer to interfere. Cross-layer photon interference then occurs within the rectangular layers however, interference of photons with different polarizations does not occur until the second stage. In this stage a series of polarizing beamsplitters in the form of an array of Mach-Zehnder-like interferometers causes photons of all polarizations to interfere [15].

Jiuzhang 1.0 generated over 50 million binary count patterns from superconducting nano-wire click detectors in  $\approx 200$ s. The experimentalists estimated it would take Fugaku, the largest supercomputer at the time, 600 million years to generate the same number of samples using the fastest exact classical algorithm at the time [20]. Exact samplers are algorithms designed to replicate an experiment by directly sampling the Torontonian or Hafnian using a classical supercomputer. When experiments claim a quantum advantage, they typically do so by comparing the run-time of the experiment with such exact samplers.

The algorithm implemented in [20] uses a chain rule sampler that samples each mode sequentially by computing the conditional probability of observing photons in the  $k$ th mode given the photon probabilities of the previous  $k - 1$ th modes. The computational complexity of this algorithm scales as  $\mathcal{O}(N_D^3 2^{N_D})$  where  $N_D = \sum_{j=1}^M c_j$  is the total number of detected photon counts. Due to

this scaling with detected counts and system size, more recent experiments aim to beat these exact samplers by increasing the number of observed counts. The mean number of counts per pattern in Jiuzhang 1.0 was  $\approx 41$ , and the largest number of counts in a single pattern was 76.

Shortly after this initial experiment, in order to reduce the probability of an exact sampler replicating the experiment, Zhong et al. [16] implemented an even larger GBS network, named Jiuzhang 2.0, which increased the number of modes to  $M = 144$ . The general fabrication process of the network remained largely the same as Jiuzhang 1.0, although the number of interferometer layers and optical elements increased. Multiple experiments were performed for different input laser powers and waists, producing an increase in the number of observed clicks, with a mean click rate of  $\approx 68$  and a maximum observed click number of  $N_D = 113$ .

At the same time, in classical computing, the increased probability of multiple photons arriving at the same detector was exploited by Bulmer et al. [22] to improve the scaling of the chain rule sampler, achieving  $\mathcal{O}(N_D^3 2^{N_D/2})$  for GBS with both PNR and click detectors. Despite this apparently modest improvement, it was estimated that generating the same number of samples as Jiuzhang 1.0 on Fugaku would now only take  $\sim 73$  days [22]. Due to the substantial speed-up over previous exact algorithms [20, 21], it was predicted that experiments using either PNR or click detectors needed  $N_D \gtrsim 100$  to surpass exact samplers [22].

To reduce the probability of multiple photons arriving at a single detector, Deng et al. [18] added a  $1 \times 8$  demux to the output modes of Jiuzhang 2.0, dubbing this upgraded network Jiuzhang 3.0. The demux is made of multiple fiber loop beamsplitters that separate photons into four temporal bins and two spatial path bins and aims to ensure  $\langle \hat{n}_j \rangle \lesssim 1$ , increasing the likelihood the click detectors are accurately counting the oncoming photons. This simple addition generated patterns with almost double the largest number of clicks obtained in Jiuzhang 2.0, with one experiment observing a maximum of  $N_D = 255$  with a mean click number of more than 100.

The linear networks implemented in the three experiments above are all static, that is, once the networks have been fabricated, one cannot reprogram any of the internal optics. This has the advantage of circumventing the exponential accumulation of loss that arises from increased depth [17, 65], although one sacrifices programmability.

To this end, Madsen et al. [17] implemented a programmable GBS called Borealis where  $N$ -squeezed state pulses are generated at a rate of 6MHz from an optical parametric oscillator in a cavity. Following from an initial proposal by Deshpande et al. [65], the linear network

is formed using three fiber delay line loops attached to a variable beamsplitter (VBS), which is constructed from a programmable phase-shifter, polarizing beamsplitters and a Pockels cell, which simply modulates the polarization. The input pulses enter each VBS sequentially, the first VBS causes pulses in the time range  $\tau = 1/(6\text{MHz})$  to interfere, which simply corresponds to interference between photons inside the VBS and the next on-coming pulse. The second and third VBS allow pulses in the range  $6\tau = 1\text{MHz}$  and  $36\tau = 6\text{MHz}$  to interfere, respectively. Photons output from the final fiber loop are then sent into a  $1 \times 16$  demux and then counted by 16 PNR detectors, which are superconducting transition edge sensors.

Transition edge sensors are a type of highly efficient PNR detector that contains a very low dark count rate [66, 67]. They extract energy information from oncoming light, where each detection event is represented as a time-varying voltage signal (see figures in Ref. [66] for an example). Therefore, the larger the number of photons in an output pulse, the larger the energy, and hence, the observed voltage signal. However, since each detector operates at some baseline temperature, a large voltage signal affects the cooldown time of each detector. To extract photon numbers from the observed voltage-time graph, Madsen et al. [17] use the method outlined in Morais et al. [66] which requires measuring the area, height, length, and maximum slope of the voltage-time output. In order to do this accurately, the detector is required to reach the cooldown temperature before an additional pulse arrives, or else one cannot distinguish between pulses.

This is achieved by the demux, which is constructed using a series of beamsplitters. The demux not only partially “dilutes” the number of photons in each output pulse, as  $c_{\text{max}} = 13$ , but it also delays the output pulses as the cooldown time for each detector is  $\approx 50 - 100\text{kHz}$  [17]. This ensures an accurate determination of photon numbers.

The two largest networks using this setup sent  $N = 216$  and  $N = 288$  input pulses into the network, detecting a mean photon number of  $\approx 125$  and  $\approx 143$ , respectively. However, this network was more susceptible to losses than the previous Jiuzhang systems [18, 25].

### 3 Simulation methods

The rapid growth of experimental networks has spurred a parallel increase in the number of algorithms proposed for the validation and/or simulation of these networks. Due to this, there are some inconsistencies in the literature on the language used to define a simulator which runs on a classical computer. Therefore, we clarify the definitions of the various classical simulators proposed for validation used throughout the rest of the review.

We first emphasize that a classical algorithm or classical simulator is any program designed to run on a digital computer, be that a standard desktop or supercomputer. The current algorithms proposed to validate GBS can be defined as either strong or weak classical simulators [68]. There is a large literature on this topic, starting from early work in quantum optics.

Weak classical simulators parallel the quantum computation of experimental networks by sampling from the output probability distribution [69]. Algorithms that sample from the full Torontonian or Hafnian distributions are exact samplers [20–22], as outlined above, and all known exact algorithms are exponentially slow. There are faster but approximate algorithms producing discrete photon count patterns that are typically called “faked” or “spoofed” patterns. Some of these generate fake patterns by sampling from the marginal probabilities of these distributions [23, 24], in which case they are called low-order marginal samplers. Such low-order methods are only approximate, since they don’t precisely simulate higher-order correlations [23, 24].

In contrast, strong classical simulators are a type of classical algorithm that evaluates the output probability distribution, be that the full or marginal probabilities, of a GBS with multiplicative accuracy, in time polynomial in the size of the quantum computation [69, 70].

Phase-space simulators have a similarity to strong classical simulators, because the samples, which are produced with a stochastic component representing quantum fluctuations, are used to compute probabilities or moments of the ideal distribution. Positive-P phase-space simulations have been widely used in quantum optics for this reason [19, 71–75]. While the sampling precision is not multiplicative, it is better than the experimental precision of GBS at the same sample number, which is sufficient for validation. By approximating the inputs as classical states, one can also use phase-space methods to produce fake patterns [32], in which case they are called a classical P-function sampler, as explained below.

For non-classical inputs, one can generate probabilities but not count patterns using phase-space methods: since there are no known algorithms to generate counts efficiently from non-classical phase-space samples.

#### 3.1 Exact classical simulation

There are a number of “exact” classical simulation methods that generate equivalent photon counts, where we use quotes for “exact,” because even these methods have round-off errors due to finite arithmetic. These algorithms are all exponentially slow [20–22]. It is known that the non-classicality of the squeezed input states of GBS is essential to providing quantum advantage in the GBS experiments, since classical states which have a positive

Glauber-Sudarshan P-representation [76, 77] are known to have classically simulable photon counts. This will be treated in Section (3.2.2). However, the non-Gaussianity arising from the photon-detection measurement process is also important.

This is because the measurement set-up where quadrature-phase-amplitude measurements are made on a system described by Gaussian states can be modeled by a positive Wigner function, and hence, becomes classically simulable [34, 35]. Gaussian states are defined as those with a Gaussian Wigner function. We note that squeezed states, while non-classical, are Gaussian states. Examples of the classical simulation of entanglement for systems with a positive Wigner function are well known [78–83].

The role of the measurement set-up in GBS is clarified by the work of Chabaud, Ferrini, Grosshans, and Markham [69] and Chabaud and Walschaers [70]. These authors illustrate a connection between quantum advantage and the non-Gaussianity of both the input states and measurement set-up. In [69], conditions sufficient for the strong simulation of Gaussian quantum circuits with non-Gaussian input states are derived. Non-Gaussian states are those for which the Gaussian factorization of correlation functions is not applicable [84].

By demonstrating a mapping between bosonic quantum computation and continuous-variable sampling computation, where the measurement comprises a double quadrature detection, Chabaud and Walschaers [70] adapt classical algorithms derived in [69] to derive a general algorithm for the strong simulation of bosonic quantum computation, which includes Gaussian boson sampling. They prove that the complexity of this algorithm scales with a measure of non-Gaussianity, the stellar rank of both the input state and measurement set-up. This enables a quantification of non-Gaussianity, including from the nature of the measurement, as a resource for achieving quantum advantage in bosonic computation.

### 3.2 Approximate classical simulation

#### 3.2.1 Low-order marginal samplers

Recent experiments have surpassed the threshold of applicability of exact samplers [16–18]. Even for experiments below this threshold [15], the computation time can still be very long and resource intensive. Therefore, approximate methods that are more readily scaled to larger sizes have been proposed. These cannot validate GBS, but they are useful in quantifying a computational advantage.

One approach presented by Villalonga et al. [23], exploits the computational efficiency of computing low-order marginal probabilities of the ideal GBS distribution to generate photon count patterns by sampling from a distribution that contains the correct low-order

marginals. We note that the relevant marginal probabilities must first be evaluated before sampling.

Two methods are implemented to compute marginals, which take the form of multivariate cumulants, also called connected correlations or Ursell functions. The first method corresponds to a Boltzmann machine (BM) and computes pattern probabilities of the form [23]

$$\langle \hat{\Pi}(\mathbf{c}) \rangle = \frac{1}{Z} \exp \left( \sum_i \lambda_i \mathfrak{Q}_1(c_i) + \sum_{i < j} \lambda_{i,j} \mathfrak{Q}_1(c_i) \mathfrak{Q}_1(c_j) + \sum_{i < j < k} \lambda_{i,j,k} \hat{\pi}_i(c_i) \hat{\pi}_j(c_j) \hat{\pi}_k(c_k) + \dots \right) \tag{14}$$

where  $Z$  is the partition function that normalizes the distribution and  $\lambda_i, \lambda_{i,j}, \dots$  are parameters computed using a mean-field approximation.

Each term in the exponent corresponds to a marginal probability of the ideal distribution, where a BM spoofer using only the first two summations was implemented due to scalability. The BM method is only applicable to GBS with click detectors, where faked binary patterns are obtained via Gibbs sampling [23].

The second method uses a greedy heuristic to generate discrete binary patterns with approximately correct second and third-order marginals. This algorithm scales exponentially with the desired order of the marginal and the length of the patterns, which are typically equal to the number of modes. Although the greedy method was originally developed for GBS with click detectors, it has since been extended to PNR detectors [17].

Faked patterns generated from both methods were compared to experimental samples from Jiuzhang 1.0 and 2.0. The best comparison results came from computing the total variation distance difference

$$\Delta \delta = \delta_m - \delta_e, \tag{15}$$

where  $\delta_m$  is the total variation distance between pattern probabilities of the ideal distribution and the marginal spoofers, and  $\delta_e$  is the total variation distance between experiment and ideal.

Since computing pattern probabilities is computationally challenging, comparisons were limited to only 14 modes. However, although the first-order BM sampler was always beaten by the experiment, faked samples generated from the second-order BM and second and third-order greedy algorithms were closer to the ideal distribution than the experiment.

Comparisons of the cross-entropy measure, which is a widely used quantum advantage benchmark in random circuit sampling quantum computers [13, 85, 86], were also performed by Villalonga et al. [23]. It remains an

open question whether this is a useful measure for boson sampling networks [24].

In general, if experimental samples obtain a smaller cross entropy than the spoofer, there is evidence of computational advantage. As was the case for the total variation distance difference, when compared to samples from the first-order BM, experimental samples were immediately larger, but for all other spoofers results were mixed, with all samples obtaining a similar cross entropy to the experiment [23].

An algorithm introduced by Oh et al. [24] was specifically designed to spoof the cross entropy measure of GBS networks using up to second-order marginal probabilities. This algorithm produced samples that successfully spoofed the small scale test networks in Ref. [17], but became too computationally demanding to spoof larger scale networks that claim quantum advantage [15–17].

### 3.2.2 Classical P-function samplers

Practical implementations of GBS will inevitably produce decoherence and losses. These may arise within the network, as discussed above, or in the input states as discussed in subsection 4.2. For large enough decoherence and loss, either the inputs, outputs or both are transformed to classical states [35, 52].

For such classical states, GBS loses its quantum advantage and an efficient classical simulation is possible. This was first shown by Rahimi-Keshari et al. [34] for Fock state boson sampling and later extended to GBS by Qi et al. [35], although the fundamental ideas are much older than this [87]. In both cases, the condition for classical simulation hinges on whether the resulting phase-space output distribution, simulated using a set of experimental inputs, was non-negative. These conditions hinge on the well-known result that, for some states, the Glauber-Sudarshan and Wigner representations produce negative distributions on phase space [54, 88], which is why they are typically referred to as quasi-probability distributions.

We define any classical algorithm that samples from the output distribution of a classical state GBS as a classical GBS sampler. Although the most commonly tested classical state is the fully decoherent thermal state, it is an extreme case and has been thoroughly disproved for all current experimental networks [15–18]. However, a more realistic scenario is a classical approximation to pure squeezed states.

Two such states have recently been proposed called squashed and squished states [18, 89]. Unlike thermal states, which have a quadrature variance of  $\Delta_{x_j}^2 = \Delta_{y_j}^2$ , squashed and squished states maintain the unequal variances of squeezed states (see Fig. 2 for a diagram of the variances for different states). Despite this, decoherence may cause the once squeezed quadrature variance to

become  $\Delta_{x_j}^2 = 1$ , whilst  $\Delta_{y_j}^2 > 1$ . Therefore, squashed and squished states are classical states. No true squeezing occurs, since neither variance is below the vacuum limit. We note that the difference between these two states is that squished states must contain the same mean number of photons as the input squeezed state [18], whereas the squashed state photon number can vary.

Comparisons of all experimental networks with simulated thermal states have, expectedly, failed [15–18]. However, Jiuzhang 1.0 data was shown to have a large degree of input decoherence [30], and hence simulated squashed states were shown to model samples from Jiuzhang 1.0 as well as the theoretical ideal distribution for some statistical tests [89]. An efficient phase-space sampler, which can generate binary patterns for any classical input state, later showed that squashed state count patterns were closer to the simulated ideal distribution than the experimental data set in Jiuzhang 2.0 that claims quantum advantage [32]. This method is reviewed in more detail in section 4. The most recent GBS experiments with PNR and click detectors, Borealis and Jiuzhang 3.0, produced outputs that were closer to the ideal than simulated squashed and squished states, although squished states have only been tested against samples from Jiuzhang 3.0 to date.

The classical GBS samplers implemented in these tests assume either all  $N \subset M$  inputs or all  $M$  outputs are classical states. A more physically realistic scenario is one where the inputs and/or outputs are mixtures of classical and quantum states. In order to model this, a classical sampler that scales with the loss rate  $\eta$  of the linear network was introduced by Oh et al. [25].

The aim of this algorithm is to simulate the output covariance matrix  $V_p$  of a pure squeezed state GBS using a tensor network method. This covariance matrix arises from a decomposition of the actual output covariance matrix  $V = W + V_p$ , where  $W \geq 0$  is a random displacement matrix arising from classical photons in the outputs.

As outlined in the previous subsection, the computational complexity of computing the ideal GBS, corresponding to  $V_p$  in this case, scales with the number of system modes and hence detected photons. However, only non-classical output photons contribute to this computational complexity. Therefore, if more experimental output photons are classical rather than non-classical, the matrix  $W$  will dominate the computation of  $V$  [25], which one should then be able to simulate efficiently.

This is the general principle of the algorithm implemented by Oh et al. [25], where the number of non-classical output photons is computed from the actual squeezing parameter  $s = -1/2 \ln(1 - \eta)$ . Clearly, as the loss rate increases, the non-classical photons decrease,

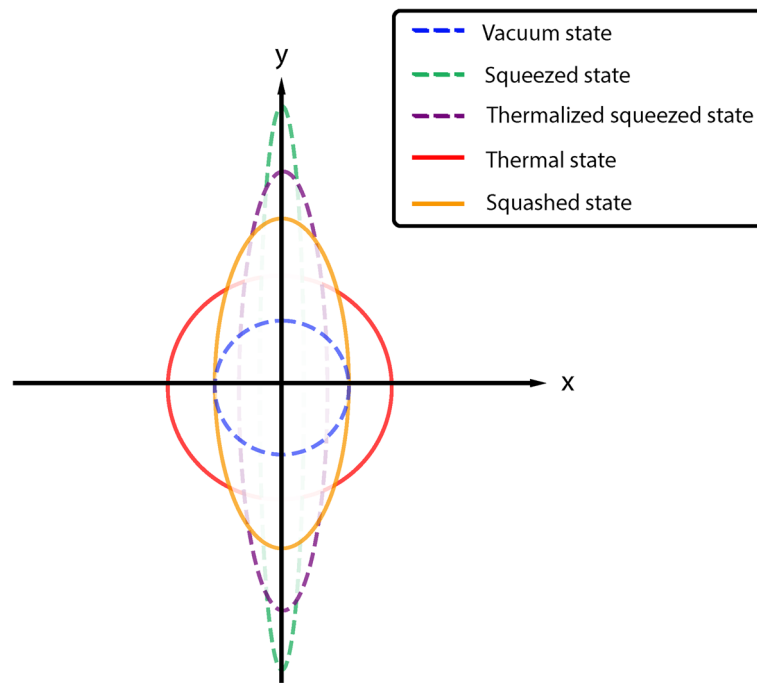


**Fig. 2** A diagram of the quadrature variance for different states. The vacuum state (blue dashed line) has variance  $\Delta_{x_j}^2 = \Delta_{y_j}^2 = 1$  and arises from the Heisenberg uncertainty principle as the minimum uncertainty state. When  $\Delta_{x_j}^2 < 1$ ,  $\Delta_{y_j}^2 > 1$  one obtains the non-classical pure squeezed state (green dashed line) or the thermalized squeezed state (purple dashed line), which has a larger variance for the squeezed quadrature than pure squeezing but remains below the vacuum limit. The classical thermal state (solid red line) has variance  $\Delta_{x_j}^2 = \Delta_{y_j}^2 > 1$ , while although the squashed state has variance  $\Delta_{x_j}^2 \neq \Delta_{y_j}^2$ , neither squeezing is below the vacuum limit as, in this case,  $\Delta_{x_j}^2 = 1$ ,  $\Delta_{y_j}^2 > 1$

in turn causing the number of classical photons to increase, allowing  $W$  to dominate the output covariance matrix.

Samples obtained from this method were used to calculate the total variation distance and cross-entropy for the small-scale test networks of Ref. [17], as well as second and higher-order cumulants for larger-scale networks [15–18]. In all cases, samples produced from this classical sampler were closer to the ideal distributions than all the experiments, highlighting the extent to which the loss rate  $\eta$  plays a role in affecting claims of quantum advantage in the current generation of GBS.

The effect of losses and noise was also investigated by Mendes et al. [90], which proposed using the Lambert-Tsallis  $W_q$ -function to determine the randomness of the observed photon counts without actually computing the output probability distribution.

The  $W_q$ -function was used to determine the randomness of output photon patterns, with counts from an  $8 \times 8$  Haar random unitary with input states having equal squeezing parameters serving as a baseline test [90]. When the input squeezing parameters and detector efficiency were altered, it was shown that one could distinguish samples from the two systems because the randomness measured by the disentropy was altered.

#### 4 Validating Gaussian boson sampling in phase space

One of the many open questions in GBS research is how to efficiently validate large-scale experimental networks. The exact methods reviewed above either suffer from scalability issues [20–22], or else they do not simulate higher-order correlations [23] due to computational complexity. Due to the rapid growth of experimental networks, even higher-order correlations will be produced due to the increase in interference pathways. The requirement of a simulation method that validates a quantum computer is that it allows the computation of measurable probabilities with an accuracy at least equal to the experimental sampling error.

Such correlations and probabilities play an increasingly important role in characterization of the output distribution [91], even when losses are present [53, 92], despite their increased sensitivity to decoherence. Therefore, scalable methods are needed that simulate higher-order correlations without performing the impractical  $\#P$ -hard direct computation of the count samples. To this end, we review recent theoretical methods that simulate grouped count probabilities (GCPs) of GBS networks using the normally ordered positive-P phase-space representation.

Currently, these methods can be used for networks with click detectors, and have successfully been applied to compare theory and experiment for samples from Jiuzhang 1.0 [30] and Jiuzhang 2.0 [32]. We emphasize that the positive P-representation does not produce discrete count patterns. However, the simulated output distributions have identical moments to the ideal GBS distributions.

We first outline the necessary background theory on phase-space representations, focusing on normally ordered methods, and GCPs before briefly reviewing simulation results for data from Jiuzhang 1.0. These results were initially presented in [30], but were obtained by simulating single-mode squeezed states as opposed to two-mode squeezed states, due to ambiguities in the public dataset. The results are corrected here, but this does not change the conclusions presented in [30], as it only has a small effect on the ideal GBS distribution comparisons and the specific fitting parameter values.

For more details on the phase-space method, the interested reader is referred to Refs. [30–32], whilst the efficient phase-space code package, xQSim, can be downloaded from public domain repositories [93].

#### 4.1 Phase-space methods

Originally developed by Wigner for symmetrically ordered operators [94], phase-space representations establish a mapping between quantum operators of different orderings to probability distributions defined on the classical phase-space variables of position and momentum [54, 95], which are more commonly rewritten in terms of the complex coherent state amplitude vectors  $\alpha, \alpha^*$ .

Moyal [96] later showed how one can use these methods to compute the dynamics of operators. Due to this, phase-space representations are frequently used to compute the operator master equation [95, 97], which for some representations, corresponds to the second-order Fokker-Planck equation (FPE), which is commonly used in statistical mechanics.

The FPE in turn, can be mapped to a stochastic differential equation (SDE) that introduces randomly fluctuating terms and, for some real or complex vector  $\mathbf{a}$ , takes the general form [98]

$$\frac{d}{dt}\mathbf{a} = \mathbf{A}(\mathbf{a}) + \mathbf{B}(\mathbf{a})\xi(t), \tag{16}$$

where  $\mathbf{A}$  is a vector function and  $\mathbf{B}$  is a matrix, both of which are typically known, while  $\xi(t)$  is a real Gaussian noise term with  $\langle \xi \rangle = 0$  and  $\langle \xi_i(t)\xi_j(t') \rangle = \delta(t - t')\delta_{ij}$ . These randomly fluctuating terms, defined as the derivative of a Wiener process [98], play an analogous role to

quantum and thermal fluctuations for applications in quantum mechanics.

Each solution of an SDE is a stochastic trajectory in phase-space and physically corresponds to a single experiment. Therefore, averages over an ensemble of trajectories  $E_S$  corresponds to a mean value from multiple experimental shots.

Such dynamical methods have been successfully applied to a variety of quantum optics systems [99–102] (also see Ref. [75] for a brief review), including the CIM [26, 27]. However, as is clear from subsection 2.2, linear networks are not modeled dynamically and hence cannot produce an SDE.

Instead, phase-space representations model linear networks as stochastic difference equations (SDFE) where the  $M$ th order SDFE takes the general form [103]

$$\mathbf{a}_{n+1} = \sum_{m=0}^M \mathbf{A}_m(n - m, \mathbf{a}_{n-m}) + \mathbf{B}(n, \mathbf{a}_n)\xi_n, \tag{17}$$

where  $\mathbf{a}_n, \mathbf{A}_m, \mathbf{B}$  and  $\xi_n$  are discrete analogs to their continuous variable definitions in Eq. (16). This becomes clearer when compared with Eq. (4).

Due to the randomly fluctuating term, SDEs do not have analytical solutions and must be computed numerically using a variety of methods [104]. As is also the case with numerical computations of non-stochastic differential equations, SDEs are approximated as difference equations for numerical computation. Although one usually has practical issues such as small step size limits for SDEs [103, 104], SDEs and SDFEs are two sides of the same coin.

Due to the use of PNR and click detectors, we focus on simulating linear networks using the normally ordered Glauber-Sudarshan diagonal P-representation and generalized P-representations. Non-normally ordered Wigner and Q-function methods are possible also [30–32], but these have too large a sampling error to be useful for simulations of photon counting.

##### 4.1.1 Generalized P-representation

The generalized P-representation developed by Drummond and Gardiner [19] is a family of normally ordered phase-space representations that produce exact and strictly positive distributions on phase-space for any quantum state. It was developed as a non-classical extension of the Glauber-Sudarshan diagonal P-representation, which is defined as

$$\hat{\rho} = \int P(\alpha)|\alpha\rangle\langle\alpha|d^{2M}\alpha,$$

where  $|\alpha\rangle$  is a coherent state vector.

Due to the absence of off-diagonal terms in the density matrix, which represent quantum superpositions, the diagonal P-representation produces a distribution  $P(\alpha)$  that is negative and singular for non-classical states such as Fock and squeezed states.

To account for this, the generalized P-representation introduces the projection operator

$$\hat{\Lambda}(\alpha, \beta) = \frac{|\alpha\rangle\langle\beta^*|}{\langle\beta^*|\alpha\rangle}, \tag{18}$$

which doubles the phase-space dimension. This increased dimension allows quantum superpositions to exist, since the basis now generates independent coherent state amplitudes  $\alpha, \beta$  with off-diagonal amplitudes  $\beta \neq \alpha^*$ , which define a quantum phase-space of larger dimensionality.

The most useful generalized-P method for simulating linear networks with squeezed state inputs is the positive P-representation, which expands the density matrix as the  $4M$ -dimensional volume integral

$$\hat{\rho} = \int \int P(\alpha, \beta) \hat{\Lambda}(\alpha, \beta) d^{2M} \alpha d^{2M} \beta. \tag{19}$$

Here,  $\alpha, \beta$  can vary along the entire complex plane and by taking the real part of Eq. (19), the density matrix becomes hermitian, thus allowing efficient sampling.

The other generalized-P method, called the complex P-representation, requires  $P(\alpha, \beta)$  to be complex, resulting from its definition as a contour integral [19]. This makes the complex P-representation useful for simulating Fock state boson sampling, which requires a complex weight term  $\Omega$  to be applied to the sampled distribution [105, 106].

One of the key reasons the positive P-representation is useful for simulating photonic networks arises from the moment relationship

$$\begin{aligned} \langle \hat{a}_{j_1}^\dagger \dots \hat{a}_{j_n} \rangle &= \langle \beta_{j_1} \dots \alpha_{j_n} \rangle_P, \\ &= \int \int P(\alpha, \beta) (\beta_{j_1} \dots \alpha_{j_n}) d^{2M} \alpha d^{2M} \beta, \end{aligned} \tag{20}$$

where  $\langle \dots \rangle$  denotes a quantum expectation value and  $\langle \dots \rangle_P$  a positive-P ensemble average. Therefore, normally ordered operator moments are exactly equivalent to positive-P phase-space moments, which is also valid for any generalized P-representation.

The reader familiar with phase-space methods may know that other representations, such as the Wigner and Husimi Q function, also output a positive, non-singular distribution for Gaussian, non-classical states.

While this is certainly true, for experiments using normally ordered detectors, one must re-order every non-normally ordered operator to obtain normal ordering. This introduces a term corresponding to vacuum noise in the initial phase-space samples, resulting in sampling errors that increase exponentially for higher-order correlations, thereby making such methods unsuitable for simulating photonic networks [32].

Using the coherent state expansion of pure squeezed states [107], one can define the input state Eq. (1) in terms of the positive P-representation as

$$\hat{\rho}^{(\text{in})} = \text{Re} \int \int P(\alpha, \beta) \hat{\Lambda}(\alpha, \beta) d\alpha d\beta. \tag{21}$$

The resulting positive-P distribution for input pure squeezed states is [30]

$$P(\alpha, \beta) = \prod_j C_j e^{-(\alpha_j^2 + \beta_j^2)(\gamma_j^{-1} + 1/2) + \alpha_j \beta_j}, \tag{22}$$

where  $C_j = \sqrt{1 + \gamma_j} / (\pi \gamma_j)$  is a normalization constant and  $\gamma_j = e^{2r_j} - 1$ .

Output samples are then readily obtained by transforming the input coherent amplitudes as  $\alpha' = T\alpha$ ,  $\beta' = T^*\beta$ , which corresponds to sampling from the output density matrix

$$\hat{\rho}^{(\text{out})} = \text{Re} \int \int P(\alpha, \beta) \hat{\Lambda}(\alpha', \beta') d\alpha d\beta. \tag{23}$$

#### 4.2 Grouped count probabilities

For GBS with click detectors, the number of possible binary patterns obtained from an experiment is  $\approx 2^M$  with each pattern having a probability of roughly  $\langle \hat{\Pi}(\mathbf{c}) \rangle \approx 2^{-M}$ . Samples from large scale networks are exponentially sparse, requiring binning to obtain meaningful statistics. It is therefore necessary to define a grouped count observable that corresponds to an experimentally measurable quantity.

The most general observable of interest is a  $d$ -dimensional grouped count probability (GCP), defined as [30]

$$\mathcal{G}_S^{(n)}(\mathbf{m}) = \left\langle \prod_{j=1}^d \left[ \sum_{\sum c_i = m_j} \hat{\Pi}_{S_j}(\mathbf{c}) \right] \right\rangle, \tag{24}$$

which is the probability of observing  $\mathbf{m} = (m_1, \dots, m_d)$  grouped counts of output modes  $\mathbf{M} = (M_1, M_2, \dots)$  contained within disjoint subsets  $S = (S_1, S_2, \dots)$ . Here, similar to Glauber's original definition from intensity correlations [87],  $n = \sum_{j=1}^d M_j \leq M$  is the GCP correlation order.

Each grouped count  $m_j$  is obtained by summing over binary patterns  $\mathbf{c}$  for modes contained within a subset  $S_j$ . For example, a  $d = 1$  dimensional GCP, typically called total counts, generates grouped counts as  $m_j = \sum_i^M c_i$ , whilst  $d > 1$  gives  $\mathbf{m} = (m_1 = \sum_{i=1}^{M/d} c_i, \dots, m_d = \sum_{i=M/d+1}^M c_i)$ . This definition also includes more traditional low-order marginal count probabilities and moments.

Although a variety of observables can be generated using GCPs, such as the marginal probabilities commonly used by spoofing algorithms [23, 24], multi-dimensional GCPs are particularly useful for comparisons with experiment. The increased dimension causes the number of grouped counts to grow, e.g. for  $d = 2$   $\mathbf{m} = (m_1, m_2)$ , which in turn increases the number of count bins (data points) available for comparisons, providing a fine grained comparison of results. This also causes effects of higher order correlations to become more statistically significant in the data [32].

One the most useful applications arises by randomly permuting the modes within each subset  $S_j$ , which results in a different grouped count for each permutation. The number of possible permutation tests scales as [32]

$$\binom{M}{M/d} = \frac{M!}{d(M/d)!(M - M/d)!}, \tag{25}$$

where different correlations are compared in each comparison test. This leads to a very large number of distinct tests, making good use of the available experimental data.

Despite these advantages, caution must be taken when comparing very high dimensional GCPs, since the increased number of bins means that there are fewer counts per bin. This causes the experimental sampling errors to increase, reducing the significance of statistical tests [32].

### 5 Computational phase-space methods

To simulate GCPs in phase space, input stochastic amplitudes  $\alpha, \beta$  corresponding to the phase-space distribution of the input state  $\hat{\rho}^{(\text{in})}$  must first be generated. However, although pure squeezed states are the theoretical ‘‘gold standard’’ of GBS, practically they are challenging to create in a laboratory and inevitably decoherence will arise from equipment.

#### 5.1 Decoherent input states

A more realistic model is one that includes decoherence in the input state. Such a model was proposed in [30] and assumes the intensity of the input light is weakened

by a factor of  $1 - \epsilon$  while adding  $n_j^{\text{th}} = \epsilon n_j$  thermal photons per mode. The number of input photons per mode remains unchanged from the pure squeezed state definition, but the coherence of photons is now altered to  $\tilde{m} = (1 - \epsilon)m_j$ . To account for possible measurement errors, a correction factor  $t$  is also applied to the transmission matrix, to improve the fit to the simulated distribution.

The advantage of this decoherence model, which is a type of thermal squeezed state [47, 108], is that it allows a simple method for generating phase-space samples for any Gaussian state following

$$\begin{aligned} \alpha_j &= \frac{1}{2} \left( \Delta_{x_j} w_j + i \Delta_{y_j} w_{j+M} \right) \\ \beta_j &= \frac{1}{2} \left( \Delta_{x_j} w_j - i \Delta_{y_j} w_{j+M} \right), \end{aligned} \tag{26}$$

where  $\langle w_j w_k \rangle = \delta_{jk}$  are real Gaussian noises that model quantum fluctuations in each quadrature and

$$\begin{aligned} \Delta_{x_j}^2 &= 2(n_j + \tilde{m}_j) \\ \Delta_{y_j}^2 &= 2(n_j - \tilde{m}_j), \end{aligned} \tag{27}$$

are the thermal squeezed state quadrature variances.

As  $\epsilon \rightarrow 1$  the inputs become classical, since  $\Delta_{x_j}^2, \Delta_{y_j}^2 \geq 1$ , but small amounts of thermalization cause the inputs to remain non-classical described, for example, by a squeezing of  $\Delta_{x_j}^2 < 1$ . So long as the state is Gaussian, one can model a variety of inputs, both classical and non-classical, by simply varying  $\epsilon$ , where  $\epsilon = 0$  corresponds to a pure squeezed state and  $\epsilon = 1$  to a thermal state. We note that this sampling method generates single-mode states. To simulate GBS with two-mode squeezed state inputs, as is the case with the Jiuzhang experiments, the  $N$  single-mode states are interfered using the matrix  $\mathbf{B} = \bigoplus_{k=1}^{N/2} U_k$  [89], where  $U_k$  is a unitary 50/50 beamsplitter matrix.

The input stochastic samples are also straightforwardly extended to non-normally ordered representations, as outlined in detail in [30–32].

Performing the summation over binary patterns can now be efficiently simulated in phase-space using the multi-dimensional inverse discrete Fourier transform [30]

$$G_S^{(n)}(\mathbf{m}) = \frac{1}{\prod_j (M_j + 1)} \sum_{\mathbf{k}} \tilde{G}_M^{(n)}(\mathbf{k}) e^{i \sum_j k_j \theta_j m_j}, \tag{28}$$

where the Fourier observable simulates all possible correlations generated in an experimental network and is defined as

$$\tilde{\mathcal{G}}_S^{(n)}(\mathbf{k}) = \left\langle \prod_{j=1}^d \bigotimes_{i \in S_j} \left( \pi_i(0) + \pi_i(1)e^{-ik_j\theta_j} \right) \right\rangle_P. \quad (29)$$

Here,  $\theta_j = 2\pi/(M_j + 1)$ ,  $k_j = 0, \dots, M_j$  and  $\pi_j = \exp(-n'_j)(\exp(n'_j) - 1)^{c_j}$  is the positive-P click observable, obtained from the equivalence Eq. (20), where  $n'_j = \alpha'_j\beta'_j$  is the output photon number.

This simulation method is highly scalable, with observables such as  $d = 1, 2$  dimensional GCPs, first and second-order marginals taking a few minutes to simulate on a desktop computer for current experimental scales. This scalability is highlighted by simulations of total counts for much larger network sizes of up to  $M = 16,000$  modes [30], which is much larger than the current generation of GBS networks. We note however that increasing the GCP dimension to  $d \geq 4$  causes the simulations to take hours as opposed to minutes. This is not particularly limiting for current experimental networks, since  $d = 4$  is also the experimental data limit, where the increase in sampling errors from too few counts per bin reduces the accuracy of statistical tests [32].

### 5.2 Phase-space classical sampler

If classical states are input into a GBS, the network can be efficiently simulated using the diagonal P-representation, which arises as a special case of the positive P-representation if  $P(\alpha, \beta) = P(\alpha)\delta(\alpha^* - \beta)$ . Due to this, initial stochastic samples are still generated using Eq. (26), except now one has rotated to a classical phase-space with  $\beta = \alpha^*$ .

Similar to non-classical states, the input density matrix for any classical state is defined as

$$\hat{\rho}^{(\text{in})} = \int P(\alpha)|\alpha\rangle\langle\alpha|d^2\alpha, \quad (30)$$

where the form of the distribution  $P(\alpha)$  changes depending on the state. Input amplitudes are again transformed to outputs following  $\alpha' = T\alpha$  or  $\alpha' = TB\alpha$  for single or two-mode states, respectively, and are used to define the output state

$$\hat{\rho}^{(\text{out})} = \int P(\alpha)|\alpha'\rangle\langle\alpha'|d^2\alpha. \quad (31)$$

Using the output coherent amplitudes, one can now efficiently generate binary patterns corresponding to any classical state input into a linear network. In order to conserve the simulated counts for each ensemble, corresponding to a single experimental shot, the  $j$ th output mode of the  $k$ th ensemble is independently and randomly sampled via the Bernoulli distribution [32]

$$p_j^{(k)}(c_j^{(\text{class})}) = (p_j^{(k)})^{c_j^{(\text{class})}} (1 - p_j^{(k)})^{1 - c_j^{(\text{class})}}. \quad (32)$$

Here,  $c_j^{(\text{class})} = 0, 1$  is the classically generated bit of the  $j$ th mode where the probability of  $c_j^{(\text{class})} = 1$ , the ‘‘success’’ probability, is

$$p_j^{(k)} = (\pi_j(1))^{(k)} = (1 - e^{-n'_j})^{(k)}. \quad (33)$$

This is simply the click probability of the  $k$ th stochastic ensemble with an output photon number of  $n'_j = |\alpha_j|^2$ .

For an  $M$ -mode network, each stochastic ensemble outputs a classical faked pattern of the form

$$(\mathbf{c}^{(\text{class})})^{(k)} = [P_1^{(k)}, P_2^{(k)}, \dots, P_M^{(k)}], \quad (34)$$

which are binned to obtain GCPs, denoted  $\mathcal{G}^{(\text{class})}$ , that can be compared to simulated distributions.

In the limit of large numbers of patterns, binned classical fakes are approximately equal to the simulated output distribution corresponding to the density matrix Eq. (31). An example of this can be seen in Fig. 3 where  $4 \times 10^6$  binary patterns are generated by sending  $N = 20$  thermal states into an  $M = N$  mode lossless linear network represented by a Haar random unitary. The binned classical patterns produce a total count distribution that agrees with simulations within sampling error, because for this classical input example, there is no quantum advantage.

### 5.3 Statistical tests

For comparisons to be meaningful, statistical tests are needed to quantify differences between experiment and theory. To this end, Refs. [30, 31] implement a slightly altered version of a standard chi-square test, which is frequently used in random number generator validation [109, 110], and is defined as

$$\chi_{ES}^2 = \sum_{i=1}^k \frac{(\mathcal{G}_{i,E} - \bar{\mathcal{G}}_{i,S})^2}{\sigma_i^2}. \quad (35)$$

Here,  $k$  is the number of valid photon count bins, which we define as a bin with more than 10 counts, and  $\bar{\mathcal{G}}_{i,S}$  is the phase-space simulated GCP ensemble mean for any input state  $S$ , which converges to the true theoretical GCP,  $\mathcal{G}_{i,S}$ , in the limit  $E_S \rightarrow \infty$ . The experimental GCP is defined as  $\mathcal{G}_{i,E}$ , and  $\sigma_i^2 = \sigma_{T,i}^2 + \sigma_{E,i}^2$  is the sum of experimental,  $\sigma_{E,i}^2$ , and theoretical,  $\sigma_{T,i}^2$ , sampling errors of the  $i$ -th bin.

The chi-square test result follows a chi-square distribution that converges to a normal distribution when  $k \rightarrow \infty$  due to the central limit theorem [111, 112]. One can use this to introduce another test that determines how many standard deviations away the comparison result is from

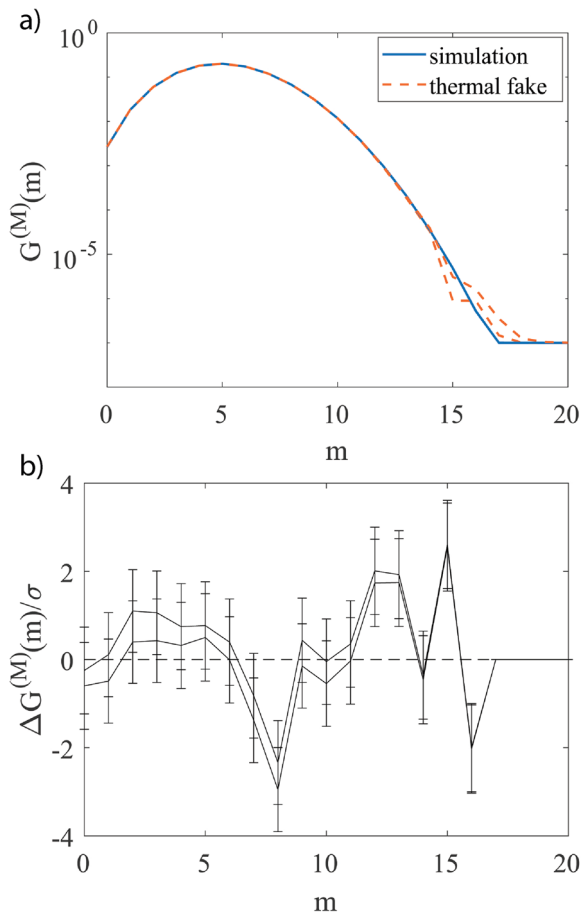


**Fig. 3** Comparisons of total counts, the  $m$  count probability regardless of pattern, for  $4 \times 10^6$  classical binary patterns generated from thermal states with  $\mathbf{r} = [1, \dots, 1]$  input into a  $20 \times 20$  Haar random unitary matrix  $\mathbf{U}$  with transmission coefficient  $t = 0.5$ . **a** Positive-P phase-space simulated output distribution, obtained using  $E_S = 1.2 \times 10^6$  ensembles, for thermal states sent into a linear network denoted by the solid blue line are compared against the distribution produced by the binned thermal fake patterns which are represented by the orange dashed line. **b** Comparison of the normalized difference  $\Delta G^{(M)}(m)/\sigma_m = (\bar{G} - G^{(\text{class})})/\sigma_m$ , where  $\sigma_m$  is the sum over compared grouped count variances (following from Eq. (35)), and  $G^{(\text{class})}$  represents a classically simulated, discrete count probability. Upper and lower lines correspond to one standard deviation of theoretical phase-space sampling errors, while the error bars correspond to the sampling errors of the simulated “fake” counts. The results are cut off for photon count bins containing less than 10 counts. The expected good agreement becomes clearer when Z-score statistical tests are performed, giving  $Z^{(\text{class})} \approx 1$ . In this example, since the input is classical there is no quantum advantage, and the classical sampler is exact, as expected

its expected normally distributed mean. The aim of this test is to obtain the probability of observing the output  $\chi_{ES}^2$  result using standard probability theory. For example, an output of  $6\sigma$ , where  $\sigma$  is the standard deviation of the

normal distribution, indicates the data has a very small probability of being observed.

To do this, Ref. [32] implemented the Z-score, or Z-statistic, test which is defined as

$$Z_{ES} = \frac{(\chi_{ES}^2/k)^{1/3} - (1 - 2/(9k))}{\sqrt{2/(9k)}}, \quad (36)$$

where  $(\chi_{ES}^2/k)^{1/3}$  is the Wilson-Hilferty (WH) transformed chi-square statistic [111], which allows a faster convergence to a normal distribution when  $k \geq 10$  [111, 112], and  $\mu = 1 - \sigma^2$ ,  $\sigma^2 = 2/(9k)$  are the corresponding mean and variance of the normal distribution.

The Z-statistic allows one to determine the probability obtaining the resulting  $\chi^2/k$  value. A result of  $Z_{ES} > 6$  would indicate that experimental distributions are so far from the simulated results that patterns may be displaying systematic errors. Valid experimental results with correct distributions should have  $\chi_{EI}^2/k \approx 1$ , where the subscript  $I$  denotes the ideal GBS distribution, with  $Z_{EI} \approx 1$ . For claims of quantum advantage, one must simultaneously prove that  $Z_{CI} \gg 1$ , where the subscript  $C$  denotes binary patterns from the best classical fake, such as the diagonal-P method described above. This is the ‘gold standard’ and would show that, within sampling errors, experimental samples are valid, and closer to the ideal distribution than any classical fake.

In the more realistic scenario of thermalized squeezed inputs, one may still have quantum advantage if  $Z_{ET} \approx 1$  while  $Z_{CT} \gg 1$ , where the T indicates a simulated thermalised squeezed state. Therefore, these four observables are of the most interest for comparisons of theory and experiment, and are given below.

#### 5.4 Comparisons with experiment

Throughout this section, for purposes of illustration, we primarily review comparisons of data from Jiuzhang 1.0 using two-mode squeezed state inputs. A thorough comparison of all data sets obtained in Jiuzhang 2.0 is presented elsewhere [32].

We first review comparisons of total counts, which is the probability of observing  $m$  clicks in any pattern and is usually one of the first observables experimentalists compare samples to. This is because in the limit of a large number of clicks, one can estimate the ideal distribution as a Gaussian distribution via the central limit theorem.

To simulate the ideal total counts distribution in phase-space using GCPs we let  $n = M$  and  $\mathcal{S} = \{1, 2, \dots, M\}$ , giving  $\mathcal{G}_{\{1, \dots, M\}}^{(M)}(m)$ . For Jiuzhang 1.0, one obtains a Z-statistic of  $Z_{EI} \approx 408$  for  $k = 61$  valid bins. Clearly, experimental samples are far from the ideal and indicate photon count distributions are not what would be expected from an ideal GBS.

To determine whether these differences either increase or decrease when higher-order correlations become more prevalent in the simulations, the dimension of the GCP is increased to  $d = 2$ . In this case, Jiuzhang 1.0 sees an almost doubling in  $Z$  values for comparisons with the simulated ideal distribution (see Fig. 4), where  $Z_{EI} \approx 796$  is obtained from  $k = 975$  [30]. The increase in the number of valid bins with GCP dimension causes the normal distribution of the WH transformed chi-square statistic to have a smaller variance. When compared to a single dimension, where  $k = 61$  gives  $\sigma^2 \approx 3.6 \times 10^{-3}$ , binning

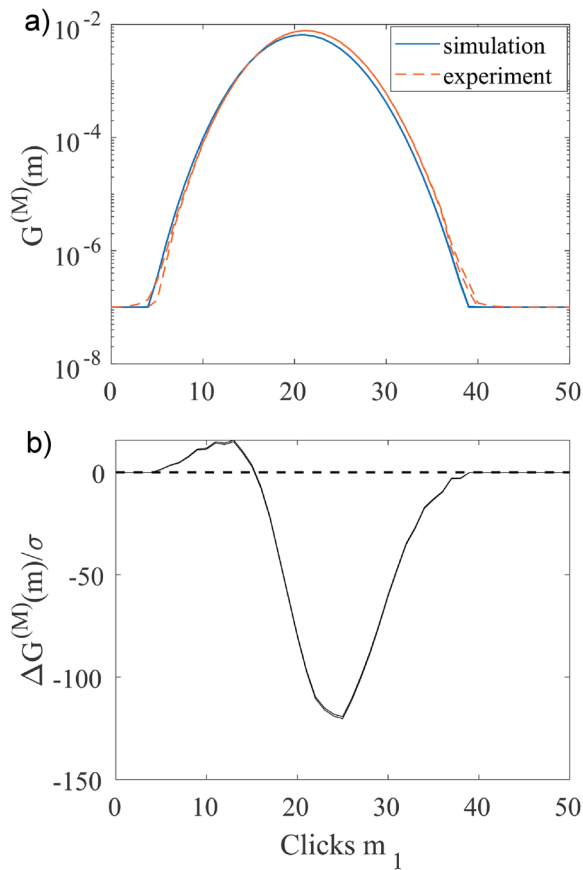


**Fig. 4** **a** Comparison of a one-dimensional planar slice through the maximum of a  $d = 2$  dimensional GCP  $\mathcal{G}_{50,50}^{(100)}(m)$  for binary patterns from Jiuzhang 1.0 data (dashed orange line). Phase-space simulations (solid blue line) are performed for the ideal GBS, without decoherence, and use  $E_S = 1.2 \times 10^6$  stochastic ensembles. **b** Normalized difference between theory and experiment  $\Delta G^{(M)}(m)/\sigma_m$  versus  $m_1$ , which is the grouped count for modes contained within the first subset  $S_1$ . Upper and lower solid black lines are  $\pm 1\sigma_T$ , with grouped count bins containing less than 10 counts being cut off. Although the distributions are visually similar in a), the normalized difference shows that significant discrepancies are present (see Fig. 3 for definitions), and one can readily determine that the ideal GBS model is not validated for this set of experimental data, although the agreement is much better if a decoherent, thermalized model is used instead

with  $d > 1$  causes experimental samples to now pass a more stringent test, as  $k = 975$  produces a normal distribution with variance  $\sigma^2 \approx 2.3 \times 10^{-4}$ .

Simulating the more realistic scenario of thermalized squeezed states, a thermalized component of  $\epsilon = 0.0811 \pm 0.0005$  and a transmission matrix correction of  $t = 1.0305 \pm 0.0005$  is used as to compare a simulated model to samples from Jiuzhang 1.0. This is very close to the original, modified parameters [30]. In this case, an order of magnitude improvement in the resulting  $Z$  value is observed, giving  $Z_{ET} \approx 17 \pm 2$  for total counts.

Despite this significant improvement, differences are still large enough that  $Z_{ET} > 1$ . Similar results were also obtained for data sets with the largest recorded photon counts in Jiuzhang 2.0, that is data sets claiming quantum advantage [32]. However, this is not the case for data sets with small numbers of recorded photons which typically give  $Z_{ET} \approx 1$  [32], although these experiments should be easily replicated by exact samplers. The large amount of apparent thermalization is the likely reason why simulated squashed states described Jiuzhang 1.0 samples just as well as the ideal GBS in Ref. [89].

When higher-order correlations are considered, samples from Jiuzhang 1.0 are far from the expected correlation moments of the ideal distribution. Although including the above fitting parameters improves this result with  $Z_{ET} \approx 130$  for  $d=2$ , the samples still deviate significantly from the theoretical thermalized distribution [30].

Unlike comparisons of total counts, samples from all data sets in Jiuzhang 2.0 satisfy  $Z_{EI}, Z_{ET} > 1$  for simulations with  $d > 1$ , meaning higher-order correlations also display significant departures from the expected theoretical results, even for the simpler cases with low numbers of photon counts [32]. The reasons for this are not currently known.

## 6 Summary

In order to effectively validate GBS quantum computers, scalable methods are needed which capture the entire interference complexity of linear networks. The positive-P phase-space representation is the only currently known method which can simulate every measurable grouped output distribution with non-classical input states, allowing efficient comparisons of theory and experiment for data that is available on a reasonable time-scale. Although it is currently limited to GBS with click detectors, an extension to GBS with PNR detectors is possible since the positive-P representation is still useful, although a different binning method is required since the outputs are no longer binary.

One of the important issues here is the extraordinary relative sparseness of the experimental data, which

makes it completely impossible to experimentally recover any reasonable estimate of the full distribution. Thus, while the full distribution is exponentially hard to compute, it is equally hard to measure. This means that comparisons of theory and experiment always involve some type of grouping or binning of the available data.

The next significant point is that one can both experimentally measure and theoretically compute the grouped distributions. This can be carried out theoretically with great precision using the positive-P phase-space simulation method, combined with a Fourier transform binning algorithm. These do not add greatly to the computational overhead, giving exact tests that are computable in just a few minutes, which is of great practical value.

The resulting statistical tests employed in these comparisons are far more scalable than ones implemented in many previous comparisons [15–18, 23–25], as they do not require the computation of photon count pattern probabilities, which limits the comparisons that can be performed using these tests. Exact simulation using direct photon counts is impractical in the large-scale regime where quantum advantage is found.

Statistical testing shows that the GBS experiments tested are far from the ideal GBS output distributions which are obtained from injecting pure squeezed vacuum states into a linear network. The reason for the discrepancy is that some form of decoherence is inevitable in such large quantum systems, and this makes the ideal standard too high a bar that is unlikely to ever be fully realized. A more reasonable goal is an output distribution obtained from including some decoherence in the inputs, although the amount of decoherence must be small enough that input states remain non-classical.

In summary, the positive P-representation provides an effective, scalable method to validate quantum photonic network data. It is not limited to quantum computing applications such as the GBS, as the theory presented here can be readily adapted to other optical networks, and can include non-ideal features that occur in practical experiments. Having a target distribution which is non-ideal yet non-classical is the “Goldilocks” target calculation of these devices: a porridge which is neither too hot nor too cold.

#### Acknowledgements

Not applicable.

#### Authors' contributions

A.S.D wrote the original draft, created figures and performed numerical simulations. All authors contributed to reviewing and editing this manuscript.

#### Funding

This research was funded through grants from NTT Phi Laboratories and the Australian Research Council Discovery Program.

#### Availability of data and materials

Phase-space GBS simulation software package xQSim can be downloaded from public domain repositories at [93].

#### Declarations

#### Competing interests

The authors declare no competing interests.

Received: 7 August 2023 Accepted: 26 October 2023

Published online: 29 November 2023

#### References

1. R.P. Feynman, Simulating physics with computers. *Int. J. Theor. Phys.* **21**, 467–488 (1982)
2. J.I. Cirac, P. Zoller, Quantum Computations with Cold Trapped Ions. *Phys. Rev. Lett.* **74**(20), 4091–4094 (1995). <https://doi.org/10.1103/PhysRevLett.74.4091>. Accessed 30 June 2023
3. J.I. Cirac, P. Zoller, A scalable quantum computer with ions in an array of microtraps. *Nature* **404**(6778), 579–581 (2000). <https://doi.org/10.1038/35007021>. Accessed 30 June 2023
4. E. Knill, R. Laflamme, G.J. Milburn, A scheme for efficient quantum computation with linear optics. *Nature* **409**, 46–52 (2001)
5. M.H. Devoret, R.J. Schoelkopf, Superconducting Circuits for Quantum Information: An Outlook. *Science* **339**(6124), 1169–1174 (2013). <https://doi.org/10.1126/science.1231930>. Accessed 30 June 2023
6. S. Aaronson, A. Arkhipov, in *Proceedings of the 43rd Annual ACM Symposium on Theory of Computing* (ACM Press, 2011), pp. 333–342
7. C.S. Hamilton, R. Kruse, L. Sansoni, S. Barkhofen, C. Silberhorn, I. Jex, Gaussian boson sampling. *Phys. Rev. Lett.* **119**, 170501 (2017). <https://doi.org/10.1103/PhysRevLett.119.170501>
8. N. Quesada, J.M. Arrazola, N. Killoran, Gaussian boson sampling using threshold detectors. *Phys. Rev. A* **98**(6), 062322 (2018)
9. Y. Yamamoto, K. Aihara, T. Leleu, K.I. Kawarabayashi, S. Kako, M. Fejer, K. Inoue, H. Takesue, Coherent Ising machines—optical neural networks operating at the quantum limit. *NPJ Quantum Inf.* **3**(1), 1–15 (2017)
10. P. Kok et al., Linear optical quantum computing with photonic qubits. *Rev. Mod. Phys.* **79**, 135–174 (2007)
11. P.L. McMahon, A. Marandi, Y. Haribara, R. Hamerly, C. Langrock, S. Tamate, T. Inagaki, H. Takesue, S. Utsunomiya, K. Aihara, R.L. Byer, M.M. Fejer, H. Mabuchi, Y. Yamamoto, A fully programmable 100-spin coherent Ising machine with all-to-all connections. *Science* **354**(6312), 614–617 (2016). <https://doi.org/10.1126/science.aah5178>
12. T. Honjo, T. Sonobe, K. Inaba, T. Inagaki, T. Ikuta, Y. Yamada, T. Kazama, K. Enbutsu, T. Umeki, R. Kasahara, K. ichi Kawarabayashi, H. Takesue, 100,000-spin coherent Ising machine. *Sci. Adv.* **7**(40), eabh0952 (2021). <https://doi.org/10.1126/sciadv.abh0952>
13. F. Arute, K. Arya, R. Babbush, D. Bacon, J.C. Bardin, R. Barends, R. Biswas, S. Boixo, F.G. Brandao, D.A. Buell et al., Quantum supremacy using a programmable superconducting processor. *Nature* **574**(7779), 505–510 (2019)
14. Y. Wu, W.S. Bao, S. Cao, F. Chen, M.C. Chen, X. Chen, T.H. Chung, H. Deng, Y. Du, D. Fan, M. Gong, C. Guo, C. Guo, S. Guo, L. Han, L. Hong, H.L. Huang, Y.H. Huo, L. Li, N. Li, S. Li, Y. Li, F. Liang, C. Lin, J. Lin, H. Qian, D. Qiao, H. Rong, H. Su, L. Sun, L. Wang, S. Wang, D. Wu, Y. Xu, K. Yan, W. Yang, Y. Yang, Y. Ye, J. Yin, C. Ying, J. Yu, C. Zha, C. Zhang, H. Zhang, K. Zhang, Y. Zhang, H. Zhao, Y. Zhao, L. Zhou, Q. Zhu, C.Y. Lu, C.Z. Peng, X. Zhu, J.W. Pan, Strong Quantum Computational Advantage Using a Superconducting Quantum Processor. *Phys. Rev. Lett.* **127**(18), 180501 (2021). <https://doi.org/10.1103/PhysRevLett.127.180501>
15. H.S. Zhong, H. Wang, Y.H. Deng, M.C. Chen, L.C. Peng, Y.H. Luo, J. Qin, D. Wu, X. Ding, Y. Hu et al., Quantum computational advantage using photons. *Science* **370**(6523), 1460–1463 (2020)
16. H.S. Zhong, Y.H. Deng, J. Qin, H. Wang, M.C. Chen, L.C. Peng, Y.H. Luo, D. Wu, S.Q. Gong, H. Su, Y. Hu, P. Hu, X.Y. Yang, W.J. Zhang, H. Li, Y. Li, X. Jiang, L. Gan, G. Yang, L. You, Z. Wang, L. Li, N.L. Liu, J.J. Renema, C.Y. Lu,

- J.W. Pan, Phase-Programmable Gaussian Boson Sampling Using Stimulated Squeezed Light. *Phys. Rev. Lett.* **127**(18), 180502 (2021). <https://doi.org/10.1103/PhysRevLett.127.180502>
17. L.S. Madsen, F. Laudenbach, M.F. Askarani, F. Rortais, T. Vincent, J.F.F. Bulmer, F.M. Miatto, L. Neuhaus, L.G. Helt, M.J. Collins, A.E. Lita, T. Gerrits, S.W. Nam, V.D. Vaidya, M. Menotti, I. Dhand, Z. Vernon, N. Quesada, J. Lavoie, Quantum computational advantage with a programmable photonic processor. *Nature* **606**(7912), 75–81 (2022). <https://doi.org/10.1038/s41586-022-04725-x>
  18. Y.H. Deng, Y.C. Gu, H.L. Liu, S.Q. Gong, H. Su, Z.J. Zhang, H.Y. Tang, M.H. Jia, J.M. Xu, M.C. Chen, H.S. Zhong, J. Qin, H. Wang, L.C. Peng, J. Yan, Y. Hu, J. Huang, H. Li, Y. Li, Y. Chen, X. Jiang, L. Gan, G. Yang, L. You, L. Li, N.L. Liu, J.J. Renema, C.Y. Lu, J.W. Pan. Gaussian Boson Sampling with Pseudo-Photon-Number Resolving Detectors and Quantum Computational Advantage (2023). Accessed 01 May 2023
  19. P.D. Drummond, C.W. Gardiner, Generalised P-representations in quantum optics. *J. Phys. A Math. Gen.* **13**(7), 2353–2368 (1980)
  20. N. Quesada, J.M. Arrazola, Exact simulation of gaussian boson sampling in polynomial space and exponential time. *Phys. Rev. Res.* **2**(2), 023005 (2020)
  21. N. Quesada, R.S. Chadwick, B.A. Bell, J.M. Arrazola, T. Vincent, H. Qi, R. García-Patrón, Quadratic Speed-Up for Simulating Gaussian Boson Sampling. *PRX Quantum* **3**(1), 010306 (2022). <https://doi.org/10.1103/PRXQuantum.3.010306>
  22. J.F.F. Bulmer, B.A. Bell, R.S. Chadwick, A.E. Jones, D. Moise, A. Rigazzi, J. Thorbecke, U.U. Haus, T. Van Vaerenbergh, R.B. Patel, I.A. Walmsley, A. Laing, The boundary for quantum advantage in Gaussian boson sampling. *Sci. Adv.* **8**(4), eabl9236 (2022). <https://doi.org/10.1126/sciadv.abl9236>
  23. B. Villalonga, M.Y. Niu, L. Li, H. Neven, J.C. Platt, V.N. Smelyanskiy, S. Boixo, Efficient approximation of experimental gaussian boson sampling. arXiv preprint [arXiv:2109.11525](https://arxiv.org/abs/2109.11525) (2021)
  24. C. Oh, L. Jiang, and B. Fefferman, Spoofing cross-entropy measure in boson sampling. *Phys. Rev. Lett.* **131**(1), 010401 (2023)
  25. C. Oh, M. Liu, Y. Alexeev, B. Fefferman, L. Jiang, Tensor network algorithm for simulating experimental gaussian boson sampling. arXiv preprint [arXiv:2306.03709](https://arxiv.org/abs/2306.03709) (2023)
  26. S. Kiesewetter, P.D. Drummond, Phase-space simulations of feedback coherent Ising machines. *Opt. Lett.* **47**(3), 649–652 (2022)
  27. S. Kiesewetter, P.D. Drummond, Coherent Ising machine with quantum feedback: The total and conditional master equation methods. *Phys. Rev. A* **106**, 022409 (2022). <https://doi.org/10.1103/PhysRevA.106.022409>
  28. Z. Wang, A. Marandi, K. Wen, R.L. Byer, Y. Yamamoto, Coherent Ising machine based on degenerate optical parametric oscillators. *Phys. Rev. A* **88**(6), 063853 (2013)
  29. A. Yamamura, K. Aihara, Y. Yamamoto, Quantum model for coherent Ising machines: Discrete-time measurement feedback formulation. *Phys. Rev. A* **96**(5), 053834 (2017)
  30. P.D. Drummond, B. Opanchuk, A. Dellios, M.D. Reid, Simulating complex networks in phase space: Gaussian boson sampling. *Phys. Rev. A* **105**(1), 012427 (2022). <https://doi.org/10.1103/PhysRevA.105.012427>
  31. A. Dellios, P.D. Drummond, B. Opanchuk, R.Y. Teh, M.D. Reid, Simulating macroscopic quantum correlations in linear networks. *Phys. Lett. A* **429**, 127911 (2022). <https://doi.org/10.1016/j.physleta.2021.127911>. Accessed 16 May 2023
  32. A.S. Dellios, B. Opanchuk, M.D. Reid, P.D. Drummond, Validation tests for GBS quantum computers using grouped count probabilities (2023). arXiv preprint [arXiv:2211.03480](https://arxiv.org/abs/2211.03480) (2022)
  33. R. Kruse, C.S. Hamilton, L. Sansoni, S. Barkhofen, C. Silberhorn, I. Jex, Detailed study of gaussian boson sampling. *Phys. Rev. A* **100**(3), 032326 (2019)
  34. S. Rahimi-Keshari, T.C. Ralph, C.M. Caves, Sufficient Conditions for Efficient Classical Simulation of Quantum Optics. *Phys. Rev. X* **6**, 021039 (2016)
  35. H. Qi, D.J. Brod, N. Quesada, R. García-Patrón, Regimes of classical simulability for noisy gaussian boson sampling. *Phys. Rev. Lett.* **124**(10), 100502 (2020)
  36. S. Aaronson, A linear-optical proof that the permanent is #p-hard. *Proc. R. Soc. Lond. A Math. Phys. Eng. Sci.* **467**(2136), 3393–3405 (2011)
  37. S. Scheel, Permanents in linear optical networks (2004). <https://arxiv.org/abs/quant-ph/0406127>
  38. M.A. Broome, A. Fedrizzi, S. Rahimi-Keshari, J. Dove, S. Aaronson, T.C. Ralph, A.G. White, Photonic boson sampling in a tunable circuit. *Science* **339**(6121), 794–798 (2013)
  39. J.B. Spring, B.J. Metcalf, P.C. Humphreys, W.S. Kolthammer, X.M. Jin, M. Barbieri, A. Datta, N. Thomas-Peter, N.K. Langford, D. Kundys, J.C. Gates, B.J. Smith, P.G.R. Smith, I.A. Walmsley, Boson Sampling on a Photonic Chip. *Science* **339**(6121), 798–801 (2013). <https://doi.org/10.1126/science.1231692>
  40. H. Wang, J. Qin, X. Ding, M.C. Chen, S. Chen, X. You, Y.M. He, X. Jiang, L. You, Z. Wang, C. Schneider, J.J. Renema, S. Höfling, C.Y. Lu, J.W. Pan, Boson Sampling with 20 Input Photons and a 60-Mode Interferometer in a 10<sup>14</sup>-Dimensional Hilbert Space. *Phys. Rev. Lett.* **123**(25), 250503 (2019). <https://doi.org/10.1103/PhysRevLett.123.250503>
  41. J. Wu, Y. Liu, B. Zhang, X. Jin, Y. Wang, H. Wang, X. Yang, A benchmark test of boson sampling on Tianhe-2 supercomputer. *Natl. Sci. Rev.* **5**(5), 715–720 (2018). <https://doi.org/10.1093/nsr/nwy079>. Accessed 26 Oct 2021
  42. D. Hangleiter, J. Eisert, Computational advantage of quantum random sampling. *Rev. Mod. Phys.* **95**, 035001 (2023)
  43. H.P. Yuen, Two-photon coherent states of the radiation field. *Phys. Rev. A* **13**(6), 2226 (1976)
  44. D. Stoler, Equivalence Classes of Minimum Uncertainty Packets. *Phys. Rev. D* **1**(12), 3217–3219 (1970). <https://doi.org/10.1103/PhysRevD.1.3217>. Accessed 23 July 2023
  45. D. Stoler, Equivalence Classes of Minimum-Uncertainty Packets. II. *Phys. Rev. D* **4**(6), 1925–1926 (1971). <https://doi.org/10.1103/PhysRevD.4.1925>. Accessed 23 July 2023
  46. D.F. Walls, Squeezed states of light. *Nature* **306**(5939), 141–146 (1983)
  47. M.S. Kim, F.A.M. de Oliveira, P.L. Knight, Properties of squeezed number states and squeezed thermal states. *Phys. Rev. A* **40**, 2494–2503 (1989). <https://doi.org/10.1103/PhysRevA.40.2494>
  48. P.D. Drummond, M. Hillery, *The quantum theory of nonlinear optics* (Cambridge University Press, 2014)
  49. P.D. Drummond, Z. Ficek (eds.), *Quantum Squeezing* (Springer-Verlag, Berlin, Heidelberg, New York, 2004)
  50. H. Vahlbruch, M. Mehmet, K. Danzmann, R. Schnabel, Detection of 15 dB squeezed states of light and their application for the absolute calibration of photoelectric quantum efficiency. *Phys. Rev. Lett.* **117**(11), 110801 (2016)
  51. M. Walschaers, *Statistical Benchmarks for Quantum Transport in Complex Systems: From Characterisation to Design*. Springer Theses (Springer International Publishing, Cham, 2018). <https://doi.org/10.1007/978-3-319-93151-7>
  52. R. García-Patrón, J.J. Renema, V. Shchesnovich, Simulating boson sampling in lossy architectures. *Quantum* **3**, 169 (2019). <https://doi.org/10.22331/q-2019-08-05-169>. [arxiv:1712.10037](https://arxiv.org/abs/1712.10037). Accessed 17 Jan 2022
  53. V. Shchesnovich, Distinguishing noisy boson sampling from classical simulations. *Quantum* **5**, 423 (2021). <https://doi.org/10.22331/q-2021-03-29-423>. [arxiv:1905.11458](https://arxiv.org/abs/1905.11458). Accessed 03 Oct 2022
  54. D. Walls, G. Milburn, *Quantum Optics* (Springer, 2008)
  55. C.K. Hong, Z.Y. Ou, L. Mandel, Measurement of subpicosecond time intervals between two photons by interference. *Phys. Rev. Lett.* **59**, 2044–2046 (1987). <https://doi.org/10.1103/PhysRevLett.59.2044>
  56. M.D. Reid, Demonstration of the Einstein-Podolsky-Rosen paradox using nondegenerate parametric amplification. *Phys. Rev. A* **40**, 913–923 (1989)
  57. A. Furusawa, J.L. Sørensen, S.L. Braunstein, C.A. Fuchs, H.J. Kimble, E.S. Polzik, Unconditional quantum teleportation. *Science* **282**(5389), 706–709 (1998)
  58. R.Y. Teh, M. Gessner, M.D. Reid, M. Fadel, Full multipartite steering inseparability, genuine multipartite steering and monogamy for continuous variable systems (2021). arXiv preprint [arXiv:2108.06926](https://arxiv.org/abs/2108.06926)
  59. J. Sperling, W. Vogel, G.S. Agarwal, True photocounting statistics of multiple on-off detectors. *Phys. Rev. A* **85**, 023820 (2012). <https://doi.org/10.1103/PhysRevA.85.023820>
  60. D. Achilles, C. Silberhorn, C. Śliwa, K. Banaszek, I.A. Walmsley, Fiber-assisted detection with photon number resolution. *Opt. Lett.* **28**(23), 2387 (2003). <https://doi.org/10.1364/OL.28.002387>. Accessed 01 Mar 2023

61. M.J. Fitch, B.C. Jacobs, T.B. Pittman, J.D. Franson, Photon-number resolution using time-multiplexed single-photon detectors. *Phys. Rev. A* **68**(4), 043814 (2003). <https://doi.org/10.1103/PhysRevA.68.043814>. Accessed 01 Mar 2023
62. J. Provaznik, L. Lachman, R. Filip, P. Marek, Benchmarking photon number resolving detectors. *Opt. Express* **28**(10), 14839 (2020). <https://doi.org/10.1364/OE.389619>. Accessed 15 Mar 2022
63. M. Reck, A. Zeilinger, H.J. Bernstein, P. Bertani, Experimental realization of any discrete unitary operator. *Phys. Rev. Lett.* **73**(1), 58–61 (1994). <https://doi.org/10.1103/PhysRevLett.73.58>. Accessed 28 Sep 2023
64. H. Wang, J. Qin, X. Ding, M.C. Chen, S. Chen, X. You, Y.M. He, X. Jiang, L. You, Z. Wang, C. Schneider, J.J. Renema, S. Höfling, C.Y. Lu, J.W. Pan, Boson sampling with 20 input photons and a 60-mode interferometer in a  $10^{14}$ -dimensional hilbert space. *Phys. Rev. Lett.* **123**, 250503 (2019)
65. A. Deshpande, A. Mehta, T. Vincent, N. Quesada, M. Hinsche, M. Ioannou, L. Madsen, J. Lavoie, H. Qi, J. Eisert, D. Hangleiter, B. Fefferman, I. Dhand, Quantum computational advantage via high-dimensional Gaussian boson sampling. *Sci. Adv.* **8**(1), eabi7894 (2022). <https://doi.org/10.1126/sciadv.abi7894>
66. L.A. Morais, T. Weinhold, M.P. de Almeida, J. Combes, A. Lita, T. Gerrits, S.W. Nam, A.G. White, G. Gillett, Precisely determining photon-number in real-time (2022). Accessed 02 Mar 2023
67. Z.H. Levine, T. Gerrits, A.L. Migdall, D.V. Samarov, B. Calkins, A.E. Lita, S.W. Nam, Algorithm for finding clusters with a known distribution and its application to photon-number resolution using a superconducting transition-edge sensor. *J. Opt. Soc. Am. B* **29**(8), 2066 (2012). <https://doi.org/10.1364/JOSAB.29.002066>. Accessed 01 Mar 2023
68. H. Pashayan, S.D. Bartlett, D. Gross, From estimation of quantum probabilities to simulation of quantum circuits. *Quantum* **4**, 223 (2020)
69. U. Chabaud, G. Ferrini, F. Grosshans, D. Markham, Classical simulation of Gaussian quantum circuits with non-Gaussian input states. *Phys. Rev. Res.* **3**(3), 033018 (2021). <https://doi.org/10.1103/PhysRevResearch.3.033018>. Accessed 23 July 2023
70. U. Chabaud, M. Walschaers, Resources for Bosonic Quantum Computational Advantage. *Phys. Rev. Lett.* **130**(9), 090602 (2023). <https://doi.org/10.1103/PhysRevLett.130.090602>. Accessed 23 July 2023
71. C.W. Gardiner, P. Zoller, *Quantum Noise*, 2nd edn. (Springer, Berlin, 2000)
72. P.D. Drummond, K. Dechoum, S. Chaturvedi, Critical quantum fluctuations in the degenerate parametric oscillator. *Phys. Rev. A* **65**, 033806 (2002)
73. P. Deuar, P.D. Drummond, Correlations in a BEC collision: first-principles quantum dynamics with 150 000 atoms. *Phys. Rev. Lett.* **98**(12), 120402 (2007)
74. P.D. Drummond, B. Opanchuk, L. Rosales-Zárate, M.D. Reid, Simulating bell violations without quantum computers. *Phys. Scr.* **2014**, 014009 (2014)
75. P.D. Drummond, S. Chaturvedi, Quantum simulations in phase-space: from quantum optics to ultra-cold physics. *Phys. Scr.* **91**(7), 073007 (2016)
76. U.M. Titulaer, R.J. Glauber, Correlation functions for coherent fields. *Phys. Rev.* **140**(3B), B676 (1965)
77. M.D. Reid, D.F. Walls, Violations of classical inequalities in quantum optics. *Phys. Rev. A* **34**(2), 1260–1276 (1986)
78. R. Graham, in *Springer Tracts in Modern Physics, Statistical theory of instabilities in stationary nonequilibrium systems with applications to lasers and nonlinear optics* (Springer, Berlin Heidelberg, 1973), pp.1–97
79. M.J. Steel, M.K. Olsen, L.I. Plimak, P.D. Drummond, S.M. Tan, M.J. Collett, D.F. Walls, R. Graham, Dynamical quantum noise in trapped Bose-Einstein condensates. *Phys. Rev. A* **58**, 4824–4835 (1998)
80. B. Opanchuk, L. Arnaud, M.D. Reid, Detecting faked continuous-variable entanglement using one-sided device-independent entanglement witnesses. *Phys. Rev. A* **89**, 062101 (2014). <https://doi.org/10.1103/PhysRevA.89.062101>
81. K.L. Ng, B. Opanchuk, M.D. Reid, P.D. Drummond, Nonlocal pair correlations in a higher-order bose gas soliton. *Phys. Rev. Lett.* **122**(20), 20604 (2019)
82. K.L. Ng, R. Polkinghorne, B. Opanchuk, P.D. Drummond, Phase-space representations of thermal bose–einstein condensates. *J. Phys. A Math. Gen.* **52**(3), 035302 (2019)
83. B. Opanchuk, L. Rosales-Zárate, R.Y. Teh, B.J. Dalton, A. Sidorov, P.D. Drummond, M.D. Reid, Mesoscopic two-mode entangled and steerable states of 40 000 atoms in a bose-einstein-condensate interferometer. *Phys. Rev. A* **100**, 060102 (2019). <https://doi.org/10.1103/PhysRevA.100.060102>
84. L. Lachman, R. Filip, Quantum non-gaussianity of light and atoms. *Prog. Quant. Electron.* **83**, 100395 (2022)
85. S. Boixo, S.V. Isakov, V.N. Smelyanskiy, R. Babbush, N. Ding, Z. Jiang, M.J. Bremner, J.M. Martinis, H. Neven, Characterizing quantum supremacy in near-term devices. *Nat. Phys.* **14**(6), 595–600 (2018)
86. S. Aaronson, S. Gunn, On the Classical Hardness of Spoofing Linear Cross-Entropy Benchmarking (2020). Accessed 30 June 2023
87. R.J. Glauber, The Quantum Theory of Optical Coherence. *Phys. Rev.* **130**, 2529–2539 (1963)
88. M. Hillery, R.F. O’Connell, M.O. Scully, E.P. Wigner, Distribution functions in physics: Fundamentals. *Phys. Rep.* **106**, 121–167 (1984)
89. J. Martínez-Cifuentes, K.M. Fonseca-Romero, N. Quesada, Classical models may be a better explanation of the Jiuzhang 1.0 Gaussian Boson Sampler than its targeted squeezed light model. *Quantum* **7**, 1076 (2023)
90. F.V. Mendes, C. Lima, R.V. Ramos, Applications of the Lambert-Tsallis Wq function in quantum photonic Gaussian boson sampling. *Quantum Inf Process* **21**(6), 215 (2022). <https://doi.org/10.1007/s11128-022-03559-w>. Accessed 27 Sep 2023
91. P.A.P. Moran, *An introduction to Probability Theory* (Clarendon Press, Oxford, 1968)
92. V. Shchesnovich, Boson sampling cannot be faithfully simulated by only the lower-order multi-boson interferences (2022). Accessed 03 Oct 2022
93. P.D. Drummond, A.S. Dellios, GitHub - peterddrummond/xqsim: Quantum network simulations in phase space (2023). <https://github.com/peterddrummond/xqsim>. Accessed 08 June 2023
94. E. Wigner, On the Quantum Correction For Thermodynamic Equilibrium. *Phys. Rev.* **40**, 749–759 (1932)
95. H.J. Carmichael, *Statistical methods in quantum optics 1. Master Equations and Fokker-Planck Equations*. (Springer, Berlin, 2002)
96. J.E. Moyal, Quantum mechanics as a statistical theory. *Math. Proc. Camb. Philos. Soc.* **45**(01), 99–124 (1949)
97. C. Gardiner, P. Zoller, *Quantum Noise: A Handbook of Markovian and Non-Markovian Quantum Stochastic Methods with Applications to Quantum Optics*. Springer Series in Synergetics (Springer, 2004). [https://books.google.com.au/books?id=a\\_xsT8oGhdgC](https://books.google.com.au/books?id=a_xsT8oGhdgC)
98. C. Gardiner, *Handbook of Stochastic Methods for Physics, Chemistry, and the Natural Sciences*. Springer complexity (Springer, 2004). <https://books.google.com.au/books?id=wLm7QgAACAAJ>
99. P.D. Drummond, C.W. Gardiner, D.F. Walls, Quasiprobability methods for nonlinear chemical and optical systems. *Phys. Rev. A* **24**, 914–926 (1981)
100. L. Rosales-Zárate, B. Opanchuk, P.D. Drummond, M.D. Reid, Probabilistic quantum phase-space simulation of bell violations and their dynamical evolution. *Phys. Rev. A* **90**, 022109 (2014)
101. R.Y. Teh, P.D. Drummond, M.D. Reid, Overcoming decoherence of schrödinger cat states formed in a cavity using squeezed-state inputs. *Phys. Rev. Res.* **2**(4), 043387 (2020)
102. R.Y. Teh, F.X. Sun, R. Polkinghorne, Q.Y. He, Q. Gong, P.D. Drummond, M.D. Reid, Dynamics of transient cat states in degenerate parametric oscillation with and without nonlinear kerr interactions. *Phys. Rev. A* **101**(4), 043807 (2020)
103. A. Rodkina, C. Kelly, On stochastic difference equations and applications (2010), pp. 1517–1520. [https://doi.org/10.1007/978-3-642-04898-2\\_568](https://doi.org/10.1007/978-3-642-04898-2_568)
104. P.E. Kloeden, E. Platen, in *Numerical Solution of Stochastic Differential Equations, Stochastic Differential Equations* (Springer Berlin Heidelberg, Berlin, Heidelberg, 1992), pp. 103–160. [https://doi.org/10.1007/978-3-662-12616-5\\_4](https://doi.org/10.1007/978-3-662-12616-5_4)
105. B. Opanchuk, L. Rosales-Zárate, M.D. Reid, P.D. Drummond, Simulating and assessing boson sampling experiments with phase-space representations. *Phys. Rev. A* **97**(4), 042304 (2018)
106. P.D. Drummond, B. Opanchuk, Initial states for quantum field simulations in phase space. *Phys. Rev. Res.* **2**(3), 033304 (2020)
107. P. Adam, I. Földesi, J. Janszky, Complete basis set via straight-line coherent-state superpositions. *Phys. Rev. A* **49**(2), 1281 (1994)

108. H. Fearn, M. Collett, Representations of squeezed states with thermal noise. *J. Mod. Opt.* **35**(3), 553–564 (1988). <https://doi.org/10.1080/09500348814550571>
109. A.L. Rukhin, J. Soto, J.R. Nechvatal, M.E. Smid, E.B. Barker, S.D. Leigh, M. Levenson, M. Vangel, D.L. Banks, et al. A statistical test suite for random and pseudorandom number generators for cryptographic applications (2010)
110. D.E. Knuth, *Art of computer programming, volume 2: Seminumerical algorithms* (Addison-Wesley Professional, New York, 2014)
111. E.B. Wilson, M.M. Hilferty, The Distribution of Chi-Square. *Proc. Natl. Acad. Sci. U.S.A.* **17**(12), 684–688 (1931). <https://doi.org/10.1073/pnas.17.12.684>
112. N.L. Johnson, *Continuous Univariate Distributions* (Houghton Mifflin Series in Statistics (Houghton Mifflin, Boston, 1970)

### **Publisher's Note**

Springer Nature remains neutral with regard to jurisdictional claims in published maps and institutional affiliations.